



HAL
open science

Rossiter-McLaughlin detection of the 9-month period transiting exoplanet HIP41378 d

A. Santerne, V. Bourrier, X. Dumusque, A. H. M. J. Triaud, L. Malavolta, V. Kunovac, D. J. Armstrong, O. Attia, S. C. C. Barros, I. Boisse, et al.

► **To cite this version:**

A. Santerne, V. Bourrier, X. Dumusque, A. H. M. J. Triaud, L. Malavolta, et al.. Rossiter-McLaughlin detection of the 9-month period transiting exoplanet HIP41378 d. *aap*, 2022, 668, pp.A172. 10.1051/0004-6361/202244182 . hal-03953778

HAL Id: hal-03953778

<https://amu.hal.science/hal-03953778>

Submitted on 26 Jan 2023

HAL is a multi-disciplinary open access archive for the deposit and dissemination of scientific research documents, whether they are published or not. The documents may come from teaching and research institutions in France or abroad, or from public or private research centers.

L'archive ouverte pluridisciplinaire **HAL**, est destinée au dépôt et à la diffusion de documents scientifiques de niveau recherche, publiés ou non, émanant des établissements d'enseignement et de recherche français ou étrangers, des laboratoires publics ou privés.



Distributed under a Creative Commons Attribution 4.0 International License

Rossiter-McLaughlin detection of the 9-month period transiting exoplanet HIP41378 d

S. Grouffal¹, A. Santerne¹, V. Bourrier², X. Dumusque², A. H. M. J. Triaud⁴, L. Malavolta^{5,12}, V. Kunovac^{3,4}, D. J. Armstrong^{6,7}, O. Attia², S. C. C. Barros^{8,9}, I. Boisse¹, M. Deleuil¹, O. D. S. Demangeon^{8,9}, C. D. Dressing¹³, P. Figueira^{2,8}, J. Lillo-Box¹¹, A. Mortier^{4,10}, D. Nardiello¹², N. C. Santos^{8,9}, and S. G. Sousa⁸

¹ Aix-Marseille Univ., CNRS, CNES, Institut Origines, LAM, Marseille, France
e-mail: salome.grouffal@lam.fr

² Observatoire Astronomique de l'Université de Genève, Chemin Pegasi 51b, 1290 Versoix, Switzerland

³ Lowell Observatory, 1400 W. Mars Hill Rd., Flagstaff, AZ 86001, USA

⁴ School of Physics & Astronomy, University of Birmingham, Edgbaston, Birmingham, B15 2TT, UK

⁵ Dipartimento di Fisica e Astronomia Galileo Galilei, Vicolo Osservatorio 3, 35122 Padova, Italy

⁶ Department of Physics, University of Warwick, Coventry, CV4 7AL, UK

⁷ Centre for Exoplanets and Habitability, University of Warwick, Coventry, CV4 7AL, UK

⁸ Instituto de Astrofísica e Ciências do Espaço, Universidade do Porto, CAUP, Rua das Estrelas, 4150-762 Porto, Portugal

⁹ Departamento de Física e Astronomia, Faculdade de Ciências, Universidade do Porto, Rua do Campo Alegre, 4169-007 Porto, Portugal

¹⁰ KICC & Astrophysics Group, Cavendish Laboratory, University of Cambridge, J.J. Thomson Avenue, Cambridge CB3 0HE, UK

¹¹ Centro de Astrobiología (CAB, CSIC-INTA), Depto. de Astrofísica, ESAC campus, 28692, Villanueva de la Cañada (Madrid), Spain

¹² INAF – Osservatorio Astronomico di Padova, Vicolo dell'Osservatorio 5, 35122 Padova, Italy

¹³ Department of Astronomy, University of California, Berkeley, CA, USA

Received 3 June 2022 / Accepted 21 October 2022

ABSTRACT

The Rossiter-McLaughlin (RM) effect is a method that allows us to measure the orbital obliquity of planets, which is an important constraint that has been used to understand the formation and migration mechanisms of planets, especially for hot Jupiters. In this paper, we present the RM observation of the Neptune-sized long-period transiting planet HIP41378 d. Those observations were obtained using the HARPS-N/TNG and ESPRESSO/ESO-VLT spectrographs over two transit events in 2019 and 2022. The analysis of the data with both the classical RM and the RM Revolutions methods allows us to confirm that the orbital period of this planet is ~ 278 days and that the planet is on a prograde orbit with an obliquity of $\lambda = 57.1^{+26.4}_{-17.9}^\circ$, a value which is consistent between both methods. HIP41378 d is the longest period planet for which the obliquity has been measured so far. We do not detect transit timing variations with a precision of 30 and 100 minutes for the 2019 and 2022 transits, respectively. This result also illustrates that the RM effect provides a solution to follow up on the transit of small and long-period planets such as those that will be detected by ESA's forthcoming PLATO mission.

Key words. planetary systems – stars: individual: HIP41378 – techniques: radial velocities – techniques: spectroscopic – stars: activity

1. Introduction

Space-based exoplanet transit surveys such as the former Kepler and the upcoming PLATO missions are hunting for small and long-period (from a hundred days up to a few years) transiting planets (Borucki et al. 2010; Rauer et al. 2014). They allow the community to explore planets that formed in the outer region of the proto-planetary disk or have a different migration mechanism than close-in planets (e.g. Ford 2014, and references therein). Moreover, those planets are not intensively irradiated by their host star, significantly affected by tides, or tidally locked; as a consequence, the physics of their atmosphere as well as their primordial composition are not impacted significantly. However, those long-period exoplanets have very few transits that could be detected during the lifetime of the space surveys. Consequently, follow-up transit observations are important in order to (1) precisely constrain the orbital ephemeris and planetary parameters,

and (2) unveil transit timing variations (hereafter TTVs). From the ground, their photometric transits are challenging to detect since the events are rare, shallow, and with a duration that might exceed the time span of a night (Bryant et al. 2021). They could be detected from space with instruments such as CHEOPS (Benz et al. 2021), but these kinds of observations are more expensive and difficult to allocate.

An alternative way to follow up on transit events is through spectroscopic measurements. In particular, the Rossiter-McLaughlin (RM) effect (Holt 1893; Rossiter 1924; McLaughlin 1924) might be used to detect such transits. Gaudi & Winn (2007) found that the amplitude of the RM effect might be larger than the Keplerian orbit signal of long-period planets. In the same spirit, the RM effect might be easier to detect from the ground than the photometric transit, depending on some specific physical and dynamical properties of the system. The advantages of in-transit spectroscopic measurements over classical transit

photometry are the following: (1) ground-based high-precision photometry is rather limited for bright stars ($V \lesssim 10$) because of the seldomness of bright comparison stars, while no comparison stars are needed for the RM effect. (2) A bright Moon might also perturb the photometry in the case that the sky conditions are not photometric. RM measurements might not be significantly affected by the Moon if the stellar lines are resolved from the Moon contamination. (3) The photometric variation mainly occurs during the transit ingress and egress, which might be difficult to detect in the case of a long-duration transit from a given observatory. Full-eclipse photometric variations are relatively flat and challenging to detect. On the other hand, the full-eclipse radial-velocity variation is as large as the ingress and egress variations (Triaud 2018), and it is, therefore, easier to detect with partial coverage of the transit, except for polar orbits (e.g. Addison et al. 2013). Therefore, the RM effect offers an interesting alternative to the ground-based detection of small and long-period (hence long-duration transits) planets transiting bright stars, especially if the latter has $v \sin i_{\star} \gtrsim 5 \text{ km s}^{-1}$ for Neptune-sized planets. This is reinforced by the improved stability of the new-generation instruments, such as ESPRESSO on the Very Large Telescope (VLT; Pepe et al. 2010).

In this context, the HIP41378 planetary system presents a rare opportunity to study small and long-period exoplanets. This system is composed of at least five planets transiting around a bright ($V = 8.93$) F-type star (Vanderburg et al. 2016; Berardo et al. 2019; Becker et al. 2019). The two inner planets b and c are sub-Neptunes with well constrained periods of 15.6 and 31.7 days, respectively. The planets d, e, and f have long orbital periods based on their transit duration. The outermost planet f has been confirmed in radial velocity with an orbital period of 542 days and an unexpected low density of $0.09 \pm 0.02 \text{ g cm}^{-3}$ (Santerne et al. 2019).

Among these long-period planets, HIP41378 d has only been observed twice in transit by the *Kepler* telescope during the K2 mission: once during campaign 5 and once three years later, during campaign 18. As a result, there are 23 possible solutions for the orbital period of planet d, up to 3 yr (i.e. the two transits observed by K2 were consecutive events) with all the harmonics down to ~ 48 days (the minimum orbital period allowed during C5; Becker et al. 2019). Thanks to asteroseismology, Lund et al. (2019) derived the stellar density with high precision and deduced that the most likely orbital period for planet d, to minimise its eccentricity, is 278.36 days. However, other transit detections are needed to fully secure the orbital period. Such a detection of a small ($R_p = 3.54 \pm 0.06 R_{\oplus}$) and long-period ($P_d = 278.36$ days) exoplanet with a transit depth of only ~ 670 ppm and a transit duration of 12.5 h is challenging in photometry from the ground. As mentioned, the RM effect is an alternative way to detect the transit of this planet. Considering that the stellar rotation is $v \sin i_{\star} \sim 5.6 \text{ km s}^{-1}$ (Santerne et al. 2019), the RM amplitude is estimated at the level of 2 m s^{-1} (see Eq. (1) in Triaud 2018), which might be detectable with current instrumentation for such a bright host star. By comparison, the minimum expected radial velocity amplitude is about 0.12 m s^{-1} as reported by Santerne et al. (2019).

Moreover, the RM effect provides interesting constraints on the planet's obliquity. Observations over the last decade have shown that planets' spin-orbit angle are not necessarily aligned with their host stars (Winn et al. 2009). However, these misalignments are mostly observed for hot Jupiters whose migration processes can be the cause of the misalignment (Albrecht et al. 2012). Multiple systems such as HIP41378 tend to be aligned; although, few measurements are available. This is likely a result

of the conservation of angular momentum during protoplanetary disk formation (Albrecht et al. 2013). As of today, four multiple systems have been observed to be misaligned: Kepler-56 (Huber et al. 2013), HD 3167 (Dalal et al. 2019; Bourrier et al. 2021), K2-290 A (Hjorth et al. 2021), and π Men (Kunovac Hodžić et al. 2021). Planets in these systems have the common point to exhibit relatively short orbital periods ($P < 50$ days). The obliquity of long-period planets in multi-planetary systems remains relatively unexplored and is an important step forward in our understanding of their formation.

This paper presenting the RM detection of HIP41378 d is organised as follows. The observations and data reduction are described in Sect. 2. Section 3 presents the analysis of the RM effect with two different methods. Finally, we discuss in Sect. 4 the derived orbital period of planet d and its obliquity as well as prospects for future observations and a characterisation of the system.

2. Observations and data reduction

In order to detect a third transit of HIP41378 d and to measure its spin-orbit angle, we secured spectroscopic observations with the HARPS-N spectrograph (Cosentino et al. 2012) at the 3.6-m Telescopio Nazionale Galileo (TNG) at the Roque de Los Muchachos Observatory in the island of La Palma, Spain. Those observations were performed during the expected transit night (assuming an orbital period of ~ 278 d) of planet d on 2019 December 19 (programme ID: A40DDT4). The target was continuously observed over 6.5 h near the expected transit egress. We also secured out-of-transit observations over 1.5 h on 2019 December 22, three nights after the transit.

Since the transit duration of planet d is ~ 12.5 h (Vanderburg et al. 2016), our 2019 HARPS-N observations could only cover 40% of the transit. To improve this coverage, we observed a second transit of planet d with both the HARPS-N (programme ID: A45DDT2) and ESPRESSO (programme ID: 0109.C-0414) spectrographs. ESPRESSO (Pepe et al. 2021) is mounted on the 8.2-m ESO-VLT (VLT) at Paranal Observatory in Chile. This second transit occurred on 2022 April 01. The target was continuously monitored with both instruments over a total of 7.7 h near the expected mid-transit time. Out-of-transit data were also secured with ESPRESSO over 2.9 h on the following night. Out-of-transit observations were not secured with HARPS-N because of clouds.

To mitigate for possible high-frequency stellar noise, we used an exposure time of 900s on both instruments. The HARPS-N spectra were reduced following the method described in Dumusque et al. (2021), while the ESPRESSO data were reduced with the online pipeline (Pepe et al. 2021). The derived radial velocities are reported in the Tables A.3–A.5.

The first five, in-transit HARPS-N spectra of the 2019 transit were obtained at relatively high airmass (above $X = 1.5$) through variable thin clouds. These spectra exhibit a significantly higher photon noise (in the range $4\text{--}7 \text{ m s}^{-1}$ while the other data of the radial-velocity time series have a photon noise at the level of $2\text{--}3 \text{ m s}^{-1}$), and they were discarded from the analysis.

In 2022, the host star exhibited significant stellar variability at the level of a few m s^{-1} with a timescale of about a week (see Fig. A.1), which superimposes with the Keplerian orbit of the various planets. This leads to significant night-to-night variability limiting the use of out-of-transit data taken the night after the transit as a reference baseline for the analysis. To model the out-of-transit radial velocity variability, we also used ESPRESSO data collected as part of the monitoring programme 5105.C-0596

within 10 days centred on the transit epoch. Those monitoring data were obtained and reduced with the same method as the transit data. They are also reported in Table A.5.

3. Analysis

3.1. Classical Rossiter-McLaughlin

We analysed the in-transit HARPS-N and ESPRESSO radial velocities using the ARoME code based on the analytical model developed by Boué et al. (2013). This code models the classical RM effect assuming the radial velocities are derived by fitting a Gaussian model to the cross-correlation functions (CCFs; Baranne et al. 1996; Pepe et al. 2002) as is the case for HARPS-N and ESPRESSO. The posterior probability was sampled using a Markov chain Monte Carlo (MCMC) method as implemented into the emcee package (Foreman-Mackey et al. 2013).

We first analysed the 2019 event alone. According to the most likely orbital period (Lund et al. 2019), we expect to have observed the transit egress. The HARPS-N data reveal a jump in radial velocity within the night at the expected time of the transit egress with a difference of $3.4 \pm 1.1 \text{ m s}^{-1}$. We interpret this significant radial velocity change as the egress of planet d, since no other transiting planets are expected at that time. The out-of-transit data secured three nights after the transit exhibit an offset at the level of $0.08 \pm 0.7 \text{ m s}^{-1}$ relative to the out-of-transit data taken during the transit night. This offset is negligible.

For the MCMC analysis, we set the following as free parameters: the mid-transit epoch $T_{0,19}$, the spin-orbit angle λ , the sky-projected equatorial stellar spin velocity $v \sin i_*$, an instrumental offset, and jitter term. The period, semi-major axis, and planet-to-star radius ratio of the planet were fixed to the median values reported by Santerne et al. (2019), and were assumed for the 278-d solution for the orbital period. Since we only observed a partial transit, we fixed the orbital inclination to the median value constrained by the K2 photometry. We assumed the HARPS-N bandpass is similar to the Kepler one and we fixed the limb darkening values to the median ones in Santerne et al. (2019). Finally, three extra parameters were needed to model the RM effect in ARoME: the apparent width of the CCF σ_0 , which we fixed to 4.6 km s^{-1} ; the width of the nonrotating star line profile, which we set to $\beta_0 = 3.2 \text{ km s}^{-1}$ following the approach described in Santos et al. (2002); and the macroturbulence, which we assume to be zero. All of these values and priors are listed in Table A.1.

We ran emcee with 45 walkers of 10^5 iterations after a burn-in of 5×10^4 iterations. Following the recommendation of the emcee documentation (Foreman-Mackey et al. 2013), we tested the convergence of the MCMC using the integrated autocorrelation time that quantifies the MC error and the efficiency of the MCMC. We then derived the median and 68.3% credible intervals of the parameters that we reported in Table A.1. Based on the 2019 event only, we find that $\lambda = 40_{-44}^{+45}^\circ$, which excludes a retrograde orbit. For the transit epoch, we find that $T_{0,19} = 2\,458\,836.42 \pm 0.03$, which is fully compatible with the predicted transit epoch of 2458836.43. This leads to a non-significant transit timing variation of $5 \pm 34 \text{ min}$.

We then considered the 2022 data. Since we observed the partial transit and as no ingress and egress have been detected in the data (as expected by the ephemeris), it is difficult to confirm the detection of the RM effect. However, we detected a significant slope with a 99.73% credible interval of $[-9.9; -0.41] \text{ m s}^{-1} \text{ d}^{-1}$ on the ESPRESSO data. This slope is beyond the instrumental stability of ESPRESSO and is interpreted as

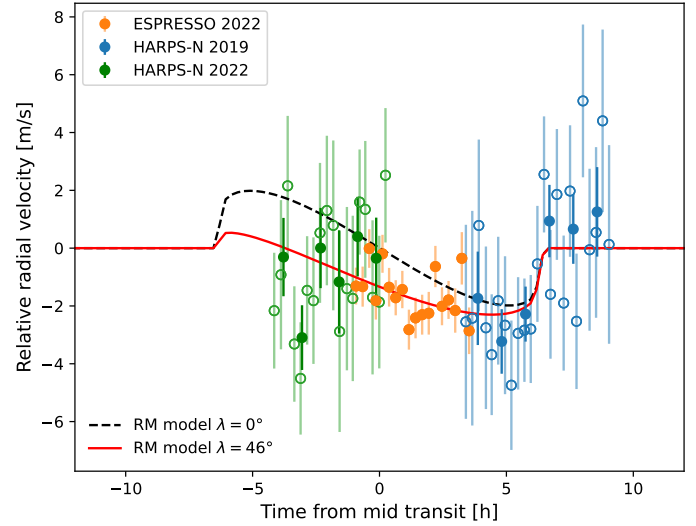


Fig. 1. RM effect for HIP41378 d. For HARPS-N 2019 (blue) and HARPS-N 2022 (green), the empty circles are the data used for the analysis, and the filled circles are the binned data. The red line is the best fit from the combined RM effect and a GP which has a projected obliquity of $\lambda = 46^\circ$. The dashed black line is the same model with a projected obliquity of $\lambda = 0^\circ$.

the signature of the RM effect. Such a slope is not present in the out-of-transit data.

We then analysed both the 2019 and 2022 events. We analysed the RM effect in the same way as was done previously, except that we set a dedicated transit epoch for the 2022 event ($T_{0,22}$). Since no significant TTVs were detected on the 2019 event, we used, as a prior for the 2022 event, a Gaussian prior centred on the expected transit epoch from Santerne et al. (2019) and a conservative width of 1 h. We also used a dedicated instrumental offset and jitter term for the HARPS-N data for both events. We set an instrumental offset and jitter term for ESPRESSO as well.

To take into account the stellar variability (with a period of ~ 8.2 days; Santerne et al. 2019) and Keplerian orbits, dominated by the orbit of HIP41378 b ($K = 1.6 \text{ m s}^{-1}$; Santerne et al. 2019), that affect the out-of-transit ESPRESSO data, we used a Gaussian process (GP) with a squared exponential kernel as follows:

$$k(\Delta t) = A \exp \left[-\frac{1}{2} \left(\frac{\Delta t}{l} \right)^2 \right], \quad (1)$$

with Δt being the time difference between data, A the amplitude of the kernel, and l the characteristic timescale. The GP was applied to ESPRESSO and HARPS-N data. The prior distribution for the new parameters and GP hyperparameters are listed in Table A.1.

We ran emcee again with 45 walkers of 10^5 iterations after a burn-in of 5×10^4 iterations. Convergence was also checked as was done previously. The derived values from the posterior distribution functions (PDFs) are reported in Table A.1. Using both events, we find that $\lambda = 46_{-37}^{+28}^\circ$ and $T_{0,22} = 2\,459\,671.53 \pm 0.06$ which leads to non-significant TTVs of $42 \pm 101 \text{ min}$ compared to the linear ephemeris.

The best-fit model of both the 2019 and 2022 events are displayed in the Fig. A.1 and phase-folded in Fig. 1. As a check, we also fitted the out-of-transit ESPRESSO data with a GP and

find that the in-transit data present a radial-velocity anomaly compatible with the RM effect (see Fig. A.2).

3.2. Rossiter-McLaughlin Revolutions

The classical analysis of the RM effect, based on the anomalous RV deviation of the disk-integrated stellar line, can yield biased and imprecise results for λ and $v \sin i_*$ (e.g. Cegla et al. 2016b; Bourrier et al. 2017). We thus performed a complementary analysis using the RM Revolutions technique (Bourrier et al. 2021), which interprets the planet-occulted stellar lines directly. This technique, however, requires that a reference spectrum can be calculated for the unocculted star, which is not possible for the 2022 HARPS-N and ESPRESSO data. The stellar line shape changed significantly between 2019 and 2022, preventing us from using the 2019 out-of-transit data as a reference for the 2022 transit. We thus focussed on the 2019 HARPS-N transit, in which post-transit exposures are available to compute the reference stellar spectrum.

Orbital and transit properties of HIP41378d are fixed to the values reported in Table A.1. Since a precise mid-transit time is essential to our analysis and no significant TTVs were found, we set its value using the nominal ephemeris from Santerne et al. (2019) in Supplementary Table 8. At the epoch of the 2019 observation, the uncertainty on the transit epoch considering a linear ephemeris is 4.6 min. This uncertainty is significantly lower than the exposure time of 15 min for each spectrum, which justifies using this value to fix the mid-transit time. We aligned the disk-integrated CCFs, CCF_{DI} , in the star rest frame, by correcting the following: (i) their radial velocities from the combined Keplerian orbits of the planets and (ii) the centroid of the master out-of-transit CCF_{DI} (master-out). Aligned CCF_{DI} were then scaled to the flux expected during the transit of HIP41378 d using a transit model using the Batman code (Kreidberg 2015), with parameters taken from Santerne et al. (2019). The CCF of the stellar disk occulted by the planet were retrieved by subtracting the scaled CCF_{DI} from the averaged out-of-transit one. Finally, they were reset to a common flux level to yield comparable intrinsic CCFs, called CCF_{intr} (see Fig. 2).

We fitted a Gaussian profile to each CCF_{intr} using `emcee`. The signal-to-noise ratio (S/N) of individual CCF_{intr} is too low to detect the resulting stellar line from the planet-occulted region. This results in broad PDFs for the line properties and prevents the derivation and interpretation of surface RVs along the transit chord with the reloaded RM approach (Cegla et al. 2016a). This highlights the interest of the RM Revolutions technique to exploit the signal from small planets. This technique indeed exploits all of the information contained in the transit time series by directly fitting a model of the stellar line to all CCF_{intr} simultaneously (details can be found in Bourrier et al. 2021). Planet-occulted stellar lines were modelled as Gaussian profiles with the same contrast, full width at half maximum (FWHM), and with centroids set by a RV model of the stellar surface assumed to rotate as a solid body. The time series of theoretical stellar lines was convolved with a Gaussian profile of width equivalent to HARPS-N resolving power, before being fitted to the CCF_{intr} map over $[-50, 50]$ km s⁻¹ in the star rest frame. Uncertainties on the CCF_{intr} were scaled with a constant factor to ensure a reduced χ^2 unity for the best fit.

We ran 40 walkers for 2000 steps, with a burn-in phase of 500 steps. These values were adjusted based on the degrees of freedom of the considered problem and the convergence of the chains. Best-fit values for the model parameters were set to the

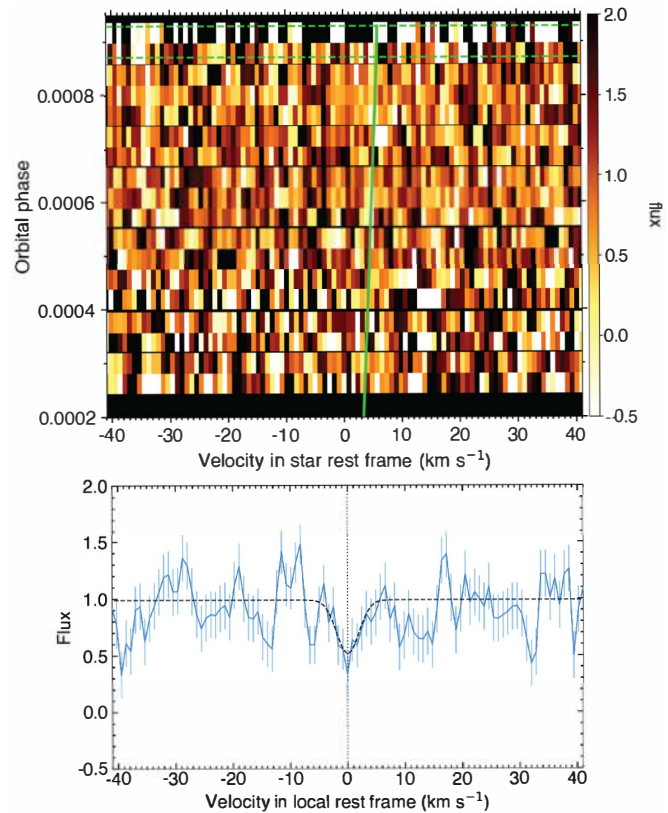


Fig. 2. Result of the RM Revolutions analysis. *Top panel:* map of the CCF_{intr} during the 2019 transit of HIP41378 d. The core of the stellar line from the planet-occulted regions is faintly visible as a brighter streak along the green line, which shows the stellar surface RV model from the RM Revolutions best fit. Egress transit contacts are shown as green dashed lines. Values are coloured as a function of the flux and plotted as a function of RV in the star rest frame (in abscissa) and orbital phase (in ordinate). *Bottom panel:* average of in-transit CCF_{intr} , after they were shifted to a common rest frame using the surface RV model. The dashed profile is the stellar line model from the RM Revolutions best fit.

median of their PDFs, and their 1σ uncertainty ranges were defined using the highest density intervals. MCMC jump parameters are the unconvolved line contrast, FWHM, λ , and $v \sin i_*$. We used uniform priors as defined in Table A.2. This yielded bimodal PDFs, with a non-physical node associated with a FWHM larger than the width of the disk-integrated line λ around 90° and $v \sin i_*$ significantly larger than the expected value. This node corresponds to the spurious dip around ~ 12 km s⁻¹ that is visible in the first CCF_{intr} that were taken at high airmass through thin clouds (see Fig. 2). To fit this feature, the MCMC needs to explore polar orbits on a fast-rotating star that is not compatible with the observed $v \sin i_*$. This solution can be naturally excluded by imposing, as a prior, that the quadratic sum of the FWHM of the CCF_{intr} , $v \sin i_*$, and the instrumental FWHM is lower than the FWHM of the CCF_{DI} , and hence 9.8 km s⁻¹.

This second fit results in the PDFs displayed in Fig. A.4. The best-fit local-line model is deeper and narrower than the disk-integrated line, as expected for this relatively fast rotator ($v \sin i_* = 6.8_{-1.0}^{+1.1}$ km s⁻¹). We derived $\lambda = 57.1_{-17.9}^{+26.4}$, which is in agreement with the classical RM analysis of the 2019 and 2019+2022 transits.

Table 1. Twenty-three possible orbital solutions for the period of HIP41378 d.

Orbital period [d]	TESS	RM	
		2019	2019+2022
1113.4465	✓	✗	✗
556.7233	✓	✓	✗
371.1488	✓	✗	✗
278.3616	✓	✓	✓
222.6893	✗	✗	✗
185.5744	✓	✓	✗
159.0638	✗	✗	✗
139.1808	✗	✓	✓
123.7163	✗	✗	✗
111.3447	✗	✓	✗
101.2224	✓	✗	✗
92.7872	✓	✓	✓
85.6497	✗	✗	✗
79.5319	✗	✓	✗
74.2298	✗	✗	✗
69.5904	✗	✓	✓
65.4969	✗	✗	✗
61.8581	✗	✓	✗
58.6024	✗	✗	✗
55.6723	✗	✓	✓
53.0213	✗	✗	✗
50.6112	✗	✓	✗
48.4107	✗	✗	✗

Notes. Values are taken from [Becker et al. \(2019\)](#). The orbital solutions that would have led to a transit during one of the sectors when TESS observed HIP41378 are indicated with ✗, while those compatible with no transit detection in TESS data have a ✓. Similarly, orbital solutions compatible with the RM detection in the 2019 event alone and both the 2019 and 2022 events have a ✓ while those that are not compatible with those observations have an ✗. The adopted solution is highlighted in bold face.

4. Discussions and conclusions

4.1. Orbital period and ephemeris

In this paper, we report spectroscopic observations during the expected transit of HIP41378 d. A transit egress was clearly detected with HARPS-N during the 2019 event exactly at the predicted time ($T_{0,19} = 2\,458\,836.42 \pm 0.03$) and predicted amplitude. We also detected the RM effect with ESPRESSO during the 2022 event that is compatible with a transit time of $T_{0,22} = 2\,459\,671.53 \pm 0.06$. Considering the 23 possible solutions for the orbital period of planet d ([Becker et al. 2019](#)), only 11 of them are compatible with the 2019 event and only five are compatible with both the 2019 and 2022 events. These solutions are listed in the Table 1. The TESS space telescope ([Ricker et al. 2015](#)) also observed HIP41378 over sectors 7, 34, 44, 45, and 46. No clear transit of planet d was detected in the public data, while the photometric precision is enough to significantly detect such an event. Considering the times of observations of TESS, only seven out of the 23 possible solutions are compatible and are listed in Table 1. Combining the three constraints, the only orbital periods of planet d that are compatible with both the TESS photometry and the RM observations are 278 and 92 days. Given a transit duration of 12.5 h, a period of 92 d would mean the orbital eccentricity of planet d is greater than 0.37 (using Eq. (5) in [Becker et al. 2019](#)), a value considered unlikely

given that all other planets are found with a low eccentricity ([Santerne et al. 2019](#)). As a consequence, we assert that the orbital period of HIP41378 d is 278 days. This solution is also the one that minimises the orbital eccentricity ([Lund et al. 2019](#)). Planet d is thus near the 3:4 mean-motion resonance (MMR) with planet e (assuming an orbital period of $P_e = 369 \pm 10$ days) and near the 1:2 MMR with planet f ($P_f = 542$ days). Based on our observations, we do not detect significant TTVs for planet d. Assuming a linear ephemeris and using the four transits detected, we expect the next mid-transit of HIP41378 d to occur on BJD = $2\,459\,949.8787 \pm 0.0077$ (2023 January 05 at 09:05 UT). The transit ingress is expected to start at BJD = $2\,459\,949.6148$ and transit egress to end at BJD = $2\,459\,950.1427$. This event could be observed by the CHEOPS space telescope.

4.2. System's obliquity

The analysis of the 2019 data with the RM Revolutions indicates that the sky-projected orbital obliquity of planet d is $\lambda = 57.1^{+26.4}_{-17.9}^\circ$, with a 99.74% credible interval of $[-14, 94]^\circ$. This result is fully compatible with the classical RM from both the 2019 and 2019+2022 events. We can reject a retrograde orbit. The marginalised PDF of λ (see Fig. A.4) exhibits a maximum that favours a nearly polar orbit. To confirm this possible misalignment, more RM observations are needed. A possibility would be to observe the RM effect of planet f, which is ~ 3 times larger than planet d, to further constrain the obliquity of this unique system.

However, other multiple systems, such as HD 3167, have planets with substantially different obliquities, up to orthogonal orbits ([Bourrier et al. 2021](#)). If the system around HIP41378 is in the same situation, we cannot use planet f to confirm the misalignment of planet d, and hence of the system. If two transiting planets in a system have different obliquities, it means we are observing them near their line of nodes. In such a case, the transit probabilities of both planets are independent, unlike for systems with low mutual inclination. As a consequence, the probability that two planets within the same system are transiting with different obliquity is the product of their transit probability. In the case of HD 3167, this probability is the following:

$$P(B \cap C) = P(B) \times P(C), \quad (2)$$

with $P(B)$ and $P(C)$ being the transit probability of planets b and c, respectively. The transit probability only depends on the geometry of the system, with $P(B) = R_*/a_b$ and $P(C) = R_*/a_c$ (assuming no eccentricity), with a_b and a_c being the semi-major axis of planets b and c, respectively. Using the values derived in [Christiansen et al. \(2017\)](#), we find that $P(B \cap C) = 0.6\%$, so the probability that both transiting planets have different obliquity is not negligible.

In the case of HIP41378, there are five transiting exoplanets and they have much longer orbital periods than the HD 3167 planets. If we assume that planets d and f might have a different obliquity, as in the HD 3167 system, then the probability that they both transit is $P(D \cap F) = 3 \times 10^{-7}$ using the values in [Santerne et al. \(2019\)](#) and it is therefore very unlikely. If we now assume that the orbits of the five planets are all independent, then the probability that those five planets are transiting is thus $P(B \cap C \cap D \cap E \cap F) = 2 \times 10^{-10}$. As a consequence, the five orbits are unlikely to be independent. This is also supported by the fact that all planets have a low mutual inclination (unlike HD 3167) below 1.5° , which is even lower when only considering the outermost planets d, e, and f whose mutual inclination is

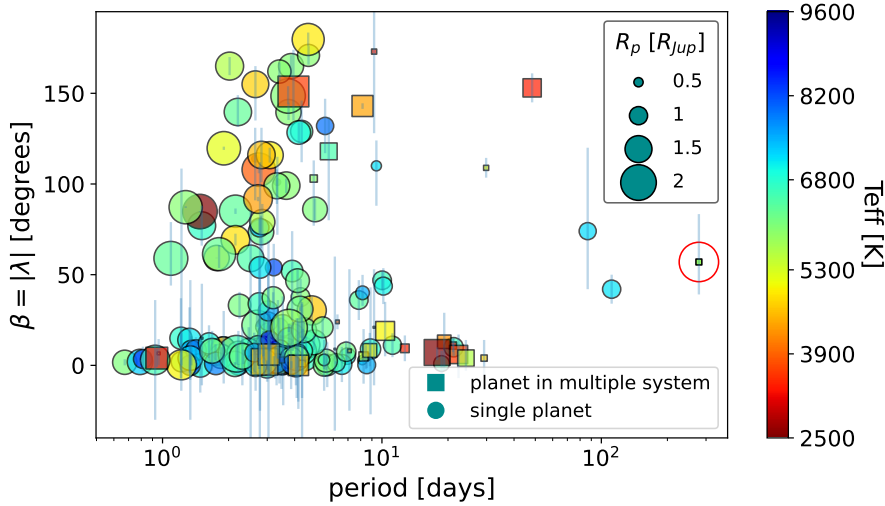


Fig. 3. Absolute value of the projected obliquity, β , as a function of the orbital periods for planets with measured obliquity. HIP41378 d is highlighted with a red circle. Planets that are part of multiple systems are represented as a square and the other with a circle. The size of the marker is scaled with the radius of the planet in Jupiter radius. The effective temperature of the host stars is represented by a colour gradient with red corresponding to relatively cool stars and blue to hot stars.

below 0.2° . This is fully compatible with the results of He et al. (2020) who found that the mutual inclination within a five-planet system such as HIP41378 is about 1.10° . This supports the idea that planets in a multi-planetary system tend to have very low mutual inclinations.

One might therefore use the obliquity of planet f to infer the one of the systems, including of planet d. Planet f has a radius 3 times larger than planet d, and hence the amplitude of the RM signal is expected to be larger (up to 30 ms^{-1}) and easier to detect than for planet d. The next opportunity to observe the transit of planet f will occur on 2022 November 13 (Alam et al. 2022).

By combining the rotation period of the star, its radius, and the value of the $v \sin i_*$ obtained with the RM Revolutions analysis, it is possible to infer the stellar inclination, that is to say the inclination of the spin axis of the star with the line of sight. The knowledge that the planets are transiting assures us that the planets are nearly edge-on and an inclined star can therefore be an indication of a misaligned system. A stellar rotation period of 6.4 ± 0.8 days has been found thanks to K2 photometry (Santerne et al. 2019) and combined with the stellar radius to obtain an equatorial rotational velocity of $10.1 \pm 1.3 \text{ km s}^{-1}$. This value is significantly different from the $v \sin i_*$ found with the RM Revolutions analysis. This lead to a stellar inclination of $i_{\star, \text{north}} = 42_{-11}^{+10}^\circ$ (with the stellar north pole facing us) and $i_{\star, \text{south}} = 138_{-9}^{+11}^\circ$ (with the stellar south pole facing us). The obliquity Ψ of the system can then be inferred from the projected obliquity λ , the stellar inclination i_s , and the planetary inclination i_p according to Fabrycky & Winn (2009):

$$\cos \Psi = \sin i_s \cos \lambda \sin i_p + \cos i_s \cos i_p. \quad (3)$$

Combining the equiprobable PDFs of Ψ_{north} and Ψ_{south} , we obtain $\Psi = 69_{-11}^{+15}^\circ$, which excludes a spin-orbit alignment.

It is surprising to have such a system with five transiting exoplanets at long orbital periods on misaligned orbits. In Fig. 3, we display all transiting exoplanets with measured obliquity from the TEPcat catalogue (Southworth 2011), highlighting the fact that HIP41378 d is the longest orbital period planet with a measured obliquity so far. Most exoplanets with already measured obliquity have short orbital periods and only a few planets in multiple systems have been observed with high obliquity. One of the reasons that is used to explain the misalignment of hot Jupiters is the high-eccentricity tidal migration (e.g. Dawson & Johnson 2018). However, planets in the HIP41378 system are

at relatively long orbital periods (the inner planet is orbiting at ~ 15 days) where tides are negligible. Since the planets are near the mean-motion resonance, it is also unlikely that they had a high-eccentricity migration. We can thus exclude this scenario as an explanation for the possible misalignment of the system.

Since the various orbits of the HIP41378 system are unlikely to be mutually inclined, a primordial mechanism, tilting the disk as a whole, may be a promising lead to explain the possible misalignment we observe (see Albrecht et al. 2022, and references therein). Although an expected result would be a rough alignment between the star and the protoplanetary disk, because they both inherit their angular momentum from the same part of a collapsing molecular cloud, some processes are able to alter this picture. Indeed, if HIP41378 formed in a dense and chaotic environment, interactions with neighbouring protostars or clumps of gas might cause an oblique infall of materials, possibly tilting the disk (Fielding et al. 2015; Bate 2018), even though this process is expected to generate moderate obliquities (Takaishi et al. 2020). Magnetic warping could also have misaligned the disk by amplifying any initial small tilt, due to the action of the Lorentz force induced by a differential rotation between the young HIP41378 star and the ionised inner disk (Foucart & Lai 2011; Romanova et al. 2021).

Alternatively, Rogers et al. (2012, 2013) argued that hot stars have photospheres that undergo random tumbling because of the propagation of internal gravity waves generated at the radiative-convective boundary. This process could have misaligned the stellar spin axis itself, leaving the orbital planes mutually aligned, but tilted with respect to the stellar equator. The feasibility of this mechanism in the case of HIP41378 is however unclear since it lies at the boundary between what is traditionally considered as cool or hot stars (e.g. Winn et al. 2010). In any case, the occasional obliquity could hardly have been damped in the past, as tidal effects have no action at such large separations.

This paper shows that the RM effect could be used to monitor the transit of small and long-period planets transiting bright stars if the latter is rotating moderately fast, similar to HIP41378. This approach could be used to measure large transit timing variations from the ground; although, it requires either the detection of the transit ingress or egress or good precision on the orbital obliquity of the system. A multi-site campaign is important to overcome the long transit duration of those planets and increase the probability of detecting a transit ingress or egress, even for planets whose transit depth is too shallow to be detected in

photometry from the ground. The RM effect could be used to measure transit time variations for the future long-period planets that the PLATO space mission (Rauer et al. 2014) will discover.

The projected obliquity found with the RM Revolutions analysis as well as the estimation of the true obliquity shows that the system is likely misaligned. The obliquity of the system has to be confirmed by a future RM detection of other planets in the system, but the obliquity determination of such a long-period and small planet is already a step forward in the understanding of the misalignment of planetary systems.

Acknowledgements. Partly based on observations made with the Italian Telescopio Nazionale *Galileo* (TNG) operated on the island of La Palma by the Fundación *Galileo* Galilei of the INAF (Istituto Nazionale di Astrofisica) at the Spanish Observatorio del Roque de los Muchachos of the Instituto de Astrofísica de Canarias. Partly based on observations collected at the European Organisation for Astronomical Research in the Southern Hemisphere under ESO programmes 0109.C-0414 and 5105.C-0596. A.S. is grateful to the astronomers on duties who performed the observations at the telescope, especially Marco Pedani (TNG) and Camila Navarrete (ESO). The project leading to this publication has received funding from the french government under the “France 2030” investment plan managed by the French National Research Agency (reference : ANR-16-CONV-000X / ANR-17-EURE-00XX) and from Excellence Initiative of Aix-Marseille University - A*MIDEX (reference AMX-21-IET-018). This work was supported by the “Programme National de Planétologie” (PNP) of CNRS/INSU. DJA acknowledges support from the STFC via an Ernest Rutherford Fellowship (ST/R00384X/1). This work was supported by FCT - Fundação para a Ciência e a Tecnologia through national funds and by FEDER through COMPETE2020 - Programa Operacional Competitividade e Internacionalização by these grants: UID/FIS/04434/2019; UIDB/04434/2020; UIDP/04434/2020; PTDC/FIS-AST/32113/2017 & POCI-01-0145-FEDER-032113; PTDC/FIS-AST/28953/2017 & POCI-01-0145-FEDER-028953. This work has been carried out in the frame of the National Centre for Competence in Research PlanetS supported by the Swiss National Science Foundation (SNSF). The authors acknowledge the financial support of the SNSF. This project has received funding from the European Research Council (ERC) under the European Union’s Horizon 2020 research and innovation programme (project SPICE DUNE, grant agreement No 947634). J.L.-B. acknowledges financial support received from “la Caixa” Foundation (ID 100010434) and from the European Unions Horizon 2020 research and innovation programme under the Marie Skłodowska-Curie grant agreement No 847648, with fellowship code LCF/BQ/PI20/11760023. This research has also been partly funded by the Spanish State Research Agency (AEI) Projects No. PID2019-107061GB-C61 and No. MDM-2017-0737 Unidad de Excelencia “María de Maeztu”- Centro de Astrobiología (INTA-CSIC). O.D.S.D. is supported in the form of work contract (DL 57/2016/CP1364/CT0004) funded by FCT. C.D. acknowledges supported provided by the David and Lucile Packard Foundation via Grant 2019-69648. S.G.S acknowledges the support from FCT through Investigador FCT contract nr. CEECIND/00826/2018 and POPH/FSE (EC). V.K. acknowledges support from NSF award AST2009501.

References

Addison, B. C., Tinney, C. G., Wright, D. J., et al. 2013, *ApJ*, **774**, L9
 Alam, M. K., Kirk, J., Dressing, C. D., et al. 2022, *ApJ*, **927**, L5
 Albrecht, S., Winn, J. N., Johnson, J. A., et al. 2012, *ApJ*, **757**, 18

Albrecht, S., Winn, J. N., Marcy, G. W., et al. 2013, *ApJ*, **771**, 11
 Albrecht, S. H., Dawson, R. I., & Winn, J. N. 2022, *PASP*, **134**, 082001
 Baranne, A., Queloz, D., Mayor, M., et al. 1996, *A&AS*, **119**, 373
 Bate, M. R. 2018, *MNRAS*, **475**, 5618
 Becker, J. C., Vanderburg, A., Rodriguez, J. E., et al. 2019, *AJ*, **157**, 19
 Benz, W., Broeg, C., Fortier, A., et al. 2021, *Exp. Astron.*, **51**, 109
 Berardo, D., Crossfield, I. J. M., Werner, M., et al. 2019, *AJ*, **157**, 185
 Borucki, W. J., Koch, D., Basri, G., et al. 2010, *Science*, **327**, 977
 Boué, G., Montalto, M., Boisse, I., et al. 2013, *A&A*, **550**, A53
 Bourrier, V., Cegla, H. M., Lovis, C., et al. 2017, *A&A*, **599**, A33
 Bourrier, V., Lovis, C., Cretignier, M., et al. 2021, *A&A*, **654**, A152
 Broeg, C., Fortier, A., Ehrenreich, D., et al. 2013, *Euro. Phys. J. Web Conf.*, **47**, 03005
 Bryant, E. M., Bayliss, D., Santerne, A., et al. 2021, *MNRAS*, **504**, L45
 Cegla, H. M., Lovis, C., Bourrier, V., et al. 2016a, *A&A*, **588**, A127
 Cegla, H. M., Oshagh, M., Watson, C. A., et al. 2016b, *ApJ*, **819**, 67
 Christiansen, J. L., Vanderburg, A., Burt, J., et al. 2017, *AJ*, **154**, 122
 Cosentino, R., Lovis, C., Pepe, F., et al. 2012, *Proc. SPIE*, **8446**, 84461V
 Dalal, S., Hébrard, G., Lecavelier des Étangs, A., et al. 2019, *A&A*, **631**, A28
 Dawson, R. I., & Johnson, J. A. 2018, *ARA&A*, **56**, 175
 Dumusque, X., Cretignier, M., Sos nowska, D., et al. 2021, *A&A*, **648**, A103
 Fabrycky, D. C., & Winn, J. N. 2009, *ApJ*, **696**, 1230
 Fielding, D. B., McKee, C. F., Socrates, A., et al. 2015, *MNRAS*, **450**, 3306
 Ford, E. B. 2014, *Proc. Natl. Acad. Science*, **111**, 12616
 Foreman-Mackey, D., Hogg, D. W., Lang, D., et al. 2013, *PASP*, **125**, 306
 Foucart, F., & Lai, D. 2011, *MNRAS*, **412**, 2799
 Gaudi, B. S., & Winn, J. N. 2007, *ApJ*, **655**, 550
 He, M. Y., Ford, E. B., Ragozzine, D., et al. 2020, *AJ*, **160**, 276
 Hjorth, M., Albrecht, S., Hirano, T., et al. 2021, *Proc. Natl. Acad. Sci.*, **118**, 2017418118
 Holt, J. R. 1893, *A&A*, **12**, 646
 Huber, D., Carter, J. A., Barbieri, M., et al. 2013, *Science*, **342**, 331
 Kreidberg, L. 2015, *PASP*, **127**, 1161
 Kunovac Hodžić, V., Triaud, A. H. M. J., Cegla, H. M., et al. 2021, *MNRAS*, **502**, 2893
 Lithwick, Y., Xie, J., & Wu, Y. 2012, *ApJ*, **761**, 122
 Lund, M. N., Knudstrup, E., Silva Aguirre, V., et al. 2019, *AJ*, **158**, 248
 McLaughlin, D. B. 1924, *ApJ*, **60**, 22
 Pepe, F., Mayor, M., Galland, F., et al. 2002, *A&A*, **388**, 632
 Pepe, F. A., Cristiani, S., Rebolo Lopez, R., et al. 2010, *Proc. SPIE*, **7735**, 77350F
 Pepe, F. A., Cristiani, S., Rebolo, R., et al. 2021, *A&A*, **645**, A96
 Rauer, H., Catala, C., Aerts, C., et al. 2014, *Exp. Astron.*, **38**, 249
 Ricker, G. R., Winn, J. N., Vanderspek, R., et al. 2015, *J. Astron. Teles. Instrum. Sys.*, **1**, 014003
 Rogers, T. M., Lin, D. N. C., & Lau, H. H. B. 2012, *ApJ*, **758**, L6
 Rogers, T. M., Lin, D. N. C., McElwaine, J. N., et al. 2013, *ApJ*, **772**, 21
 Romanova, M. M., Koldoba, A. V., Ustyugova, G. V., et al. 2021, *MNRAS*, **506**, 372
 Rossiter, R. A. 1924, *ApJ*, **60**, 15
 Santerne, A., Malavolta, L., Kosiarek, M. R., et al. 2019, *Nat Astron.*, submitted [arXiv:1911.07355]
 Santos, N. C., Mayor, M., Naef, D., et al. 2002, *A&A*, **392**, 215
 Southworth, J. 2011, *MNRAS*, **417**, 2166
 Takaishi, D., Tsukamoto, Y., & Suto, Y. 2020, *MNRAS*, **492**, 5641
 Triaud, A. H. M. J. 2018, *Handbook of Exoplanets* (Berlin: Springer), 2
 Vanderburg, A., Becker, J. C., Christiansen, M. H., et al. 2016, *ApJ*, **827**, L10
 Winn, J. N., Johnson, J. A., Fabrycky, D., et al. 2009, *ApJ*, **700**, 302
 Winn, J. N., Fabrycky, D., Albrecht, S., et al. 2010, *ApJ*, **718**, L145

Appendix A: Supplement figures and tables

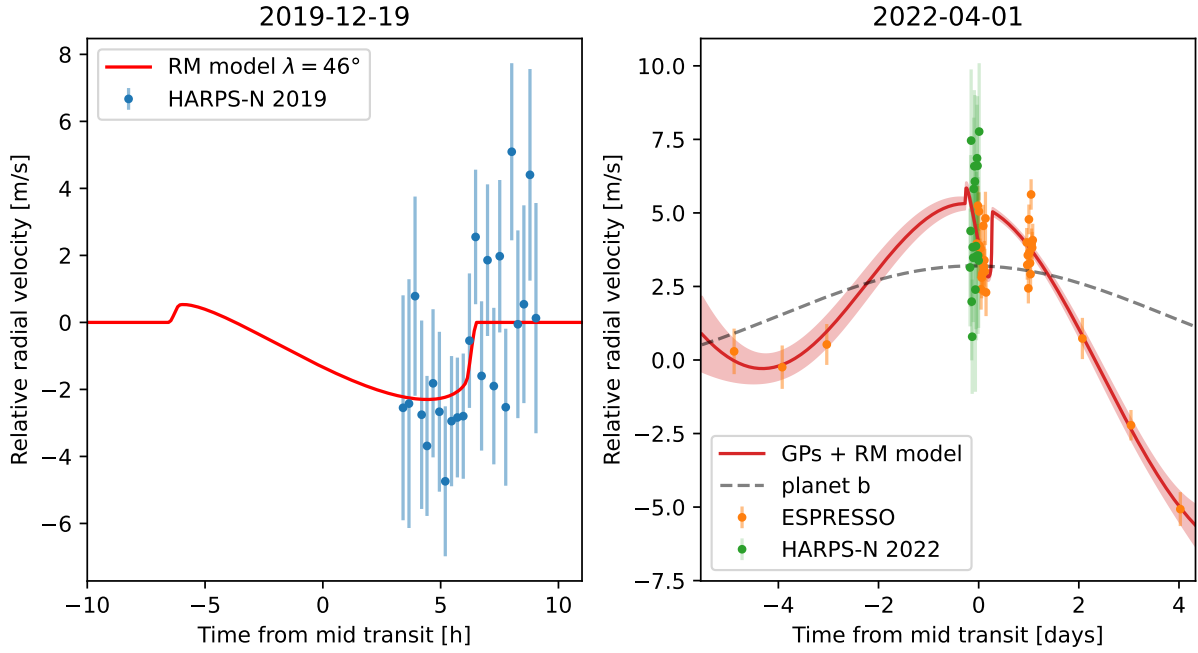


Fig. A.1. *Left panel:* HARPS-N 2019 data (blue dots) with the best-fit RM model as a red line. *Right panel:* In- and out-of-transit data from ESPRESSO (orange) and in-transit data from HARPS-N (green) for the run of 2022. The red shaded area is the combined best fit of the RM effect and a GP for the out-of-transit data from ESPRESSO. The Keplerian orbit of planet b is represented as a dashed grey line.

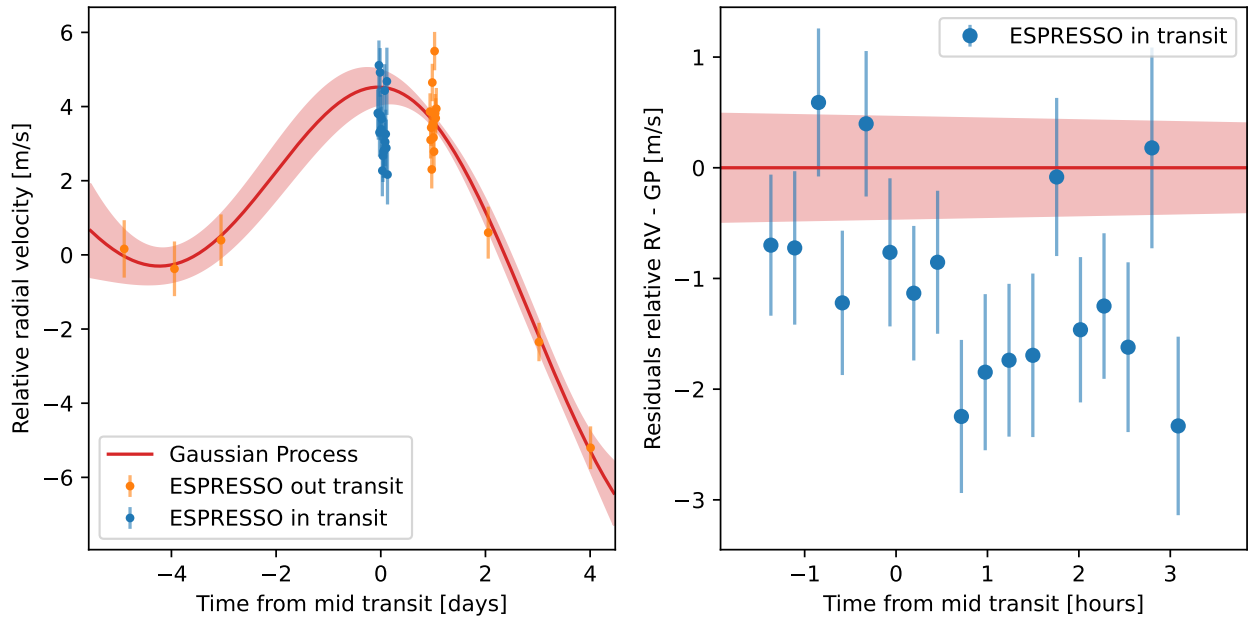


Fig. A.2. *Left panel:* Result of the GP fit (red line) to the out-of-transit ESPRESSO data (orange points). The in-transit data in blue are not taken into account for the GP fit. *Right panel:* Zoom on the residuals between the in-transit data from ESPRESSO and the GP fit to the out-of-transit data. The in-transit data show a median radial velocity anomaly of $-1.18 \pm 0.17 \text{ m s}^{-1}$ that is interpreted as the signature of the RM effect.

Table A.1. List of parameters used in the classical analysis.

Parameter model	Prior	Posterior (median and 68.3% C.I.)	
		2019	2019 + 2022
<i>Rossiter-McLaughlin model parameters</i>			
Period P_d [d]	fixed	278.3618	
Transit epoch 2019 $T_{0,19}$ [BJD - 2400000]	$\mathcal{N}(58836.4318, 0.0833)$	58836.4195 ± 0.0271	58836.4169 ± 0.0249
Transit epoch 2022 $T_{0,22}$ [BJD - 2400000]	$\mathcal{N}(59671.5049, 0.0833)$	–	59671.5279 ± 0.0634
Semi-major axis [R_*]	fixed	147.03	
Orbital inclination i_p [°]	fixed	89.81	
Projected obliquity λ [°]	$\mathcal{U}(-90, 360)$	40^{+45}_{-44}	46^{+28}_{-37}
Eccentricity [°]	fixed	0	
Limb darkening coefficient u_a	fixed	0.315	
Limb darkening coefficient u_b	fixed	0.304	
Width of the non-rotating line profile β_0 [km s^{-1}]	fixed	3.2375	
Stellar equatorial velocity $v \sin i_*$ [km s^{-1}]	$\mathcal{N}(5.5, 1)$	5.9 ± 1.4	3.8 ± 1.0
Width of the CCF σ_0 [km s^{-1}]	fixed	4.5864	
Planet radius R_p [R_*]	fixed	0.0253	
Stellar radius R_* [R_\odot]	fixed	1.28	
<i>Instrumental parameters</i>			
Jitter HARPS-N 2019 [m s^{-1}]	$\mathcal{U}(0, 10)$	0.63 ± 0.56	0.68 ± 0.59
Jitter HARPS-N 2022 [m s^{-1}]	$\mathcal{U}(0, 10)$	–	1.08 ± 0.78
Jitter ESPRESSO 2022 [m s^{-1}]	$\mathcal{U}(0, 10)$	–	0.56 ± 0.17
Offset HARPS-N 2019 [m s^{-1}]	$\mathcal{U}(50000, 51000)$	53198.08 ± 0.75	53197.72 ± 0.68
Offset HARPS-N 2022 [m s^{-1}]	$\mathcal{U}(50000, 51000)$	–	$53193.55 \pm 12.57^*$
Offset ESPRESSO 2022 [m s^{-1}]	$\mathcal{U}(50000, 51000)$	–	$50600.73 \pm 12.54^*$
<i>Gaussian Process parameters</i>			
coefficient ℓ	$\mathcal{U}(0, 100)$	–	4.0 ± 1.8
coefficient A	$\mathcal{U}(0, 100)$	–	15^{+32}_{-8}

* The relative offset between HARPS-N and ESPRESSO in 2022 is $< 1 \text{ m s}^{-1}$.

Table A.2. List of parameters used in the RM Revolutions analysis.

Parameter model	Prior	Posterior (median and 68.3% C.I.)
<i>Rossiter-McLaughlin Revolutions model parameters</i>		
FWHM [km s^{-1}]	$\mathcal{U}(0, 30)^*$	$3.8^{+1.3}_{-1.8}$
Line contrast	$\mathcal{U}(0, 1)$	0.6 ± 0.1
Projected obliquity λ [°]	$\mathcal{U}(-180, 180)$	$57.1^{+26.4}_{-17.9}$
$v \sin i_*$ [km s^{-1}]	$\mathcal{U}(0, 20)^*$	6.8 ± 1.0

* The other prior: the quadratic sum of the FWHM of the CCF_{intr}, $v \sin i_*$, and the instrumental FWHM must be lower than the FWHM of the CCF_{DI}, and hence 9.8 km s^{-1}

NOTE: All the orbital and transit parameters are fixed and taken from Santerne et al. (2019).

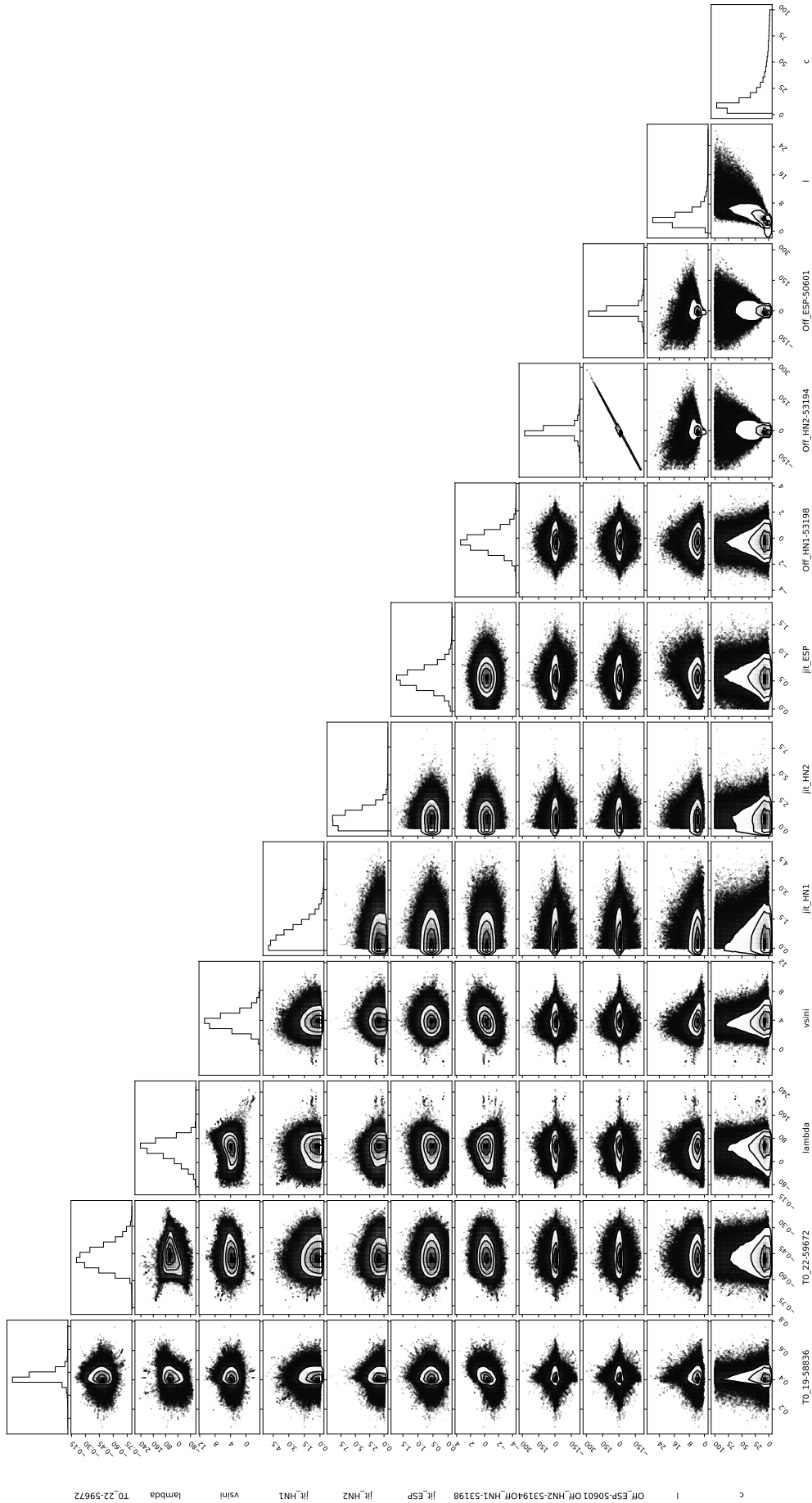


Fig. A.3. Correlation diagrams for the posterior density functions of all the parameters for the classical RM effect method. A high-resolution plot can be provided upon request.

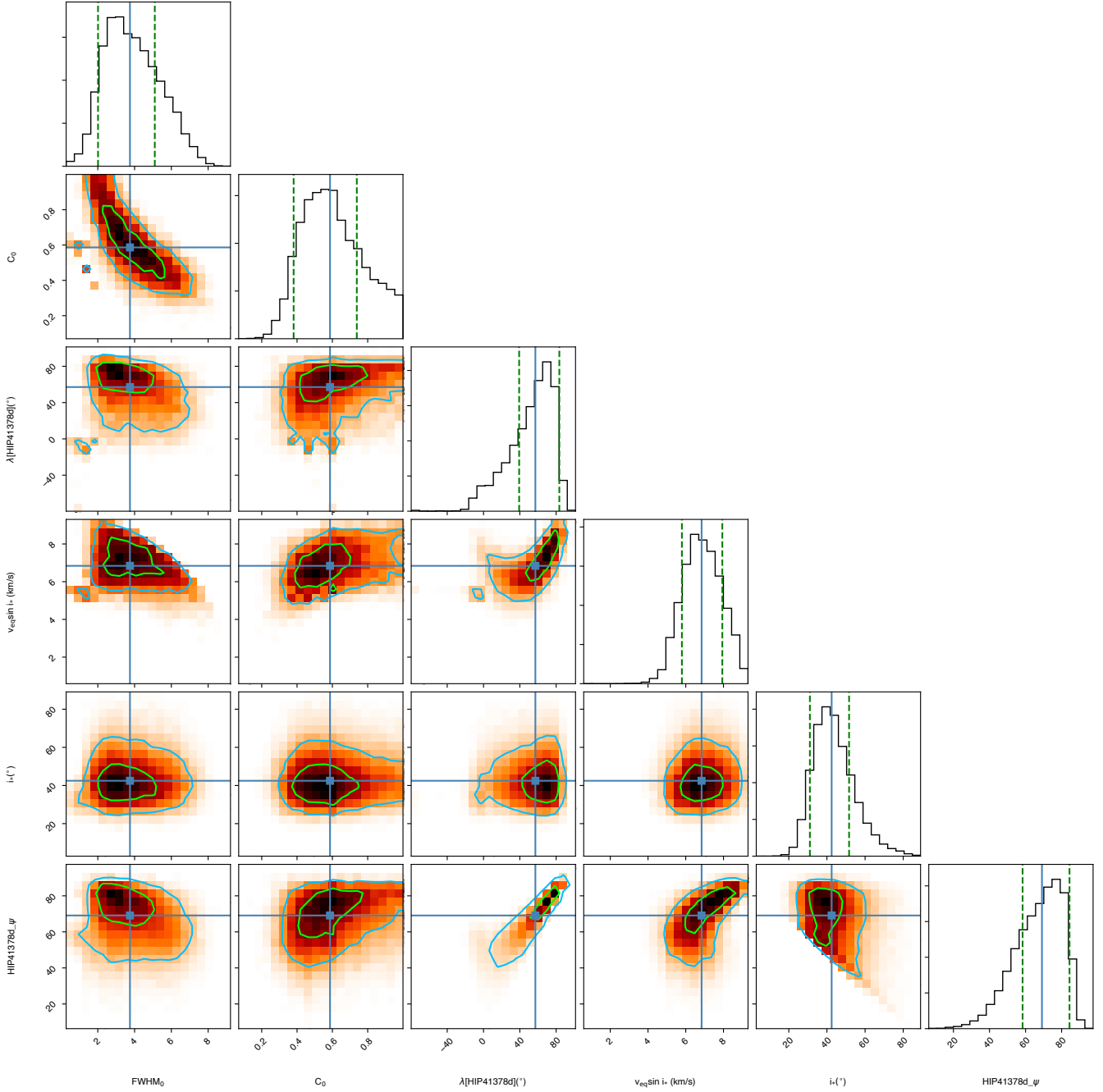


Fig. A.4. Correlation diagrams for the PDFs of the RM Revolutions model parameters: the FWHM, C_0 , λ , and $v \sin i_*$, as well as the inferred parameters i_* and Ψ . Green and blue lines show the 1 and 2σ simultaneous 2D confidence regions that contain 39.3% and 86.5% of the accepted steps, respectively. One-dimensional histograms correspond to the distributions projected on the space of each line parameter, with the green dashed lines limiting the 68.3% highest density intervals. The blue lines and squares show the median values. A high-resolution plot can be provided upon request.

Table A.3. HARPS-N 2019 radial velocity data.

Time [BJD-2400000]	RV [$m.s^{-1}$]	σ_{RV} [$m.s^{-1}$]
58836.50490*	50566.14646	6.109333
58836.51532*	50565.39129	4.403379
58836.52679*	50568.22701	5.941264
58836.53650*	50572.81001	4.941047
58836.54852*	50573.82814	7.256684
58836.55875	50562.47735	3.520979
58836.56924	50563.39081	3.972621
58836.57997	50568.51587	3.077452
58836.59164	50561.78496	2.890512
58836.60112	50560.71606	2.088641
58836.61180	50563.67220	2.216153
58836.62302	50563.62464	2.404741
58836.63342	50563.00342	2.242640
58836.64449	50562.47897	1.925289
58836.65485	50563.69707	1.762094
58836.66523	50562.71957	1.848962
58836.67617	50563.25493	1.998792
58836.68705	50567.04820	1.996846
58836.69763	50564.31770	2.238532
58836.70815	50568.54011	2.277891
58836.71927	50564.32930	2.364764
58836.72974	50567.06047	2.296536
58836.74035	50564.37499	2.373564
58836.75096	50571.49768	2.711264
58836.76181	50566.48523	2.890773
58836.77246	50565.14599	3.062877
58836.78321	50570.12908	3.308243
58836.79381	50564.80594	3.633269
58839.54026	50566.97746	2.171005
58839.55089	50566.34706	2.003333
58839.56143	50566.40512	1.960066
58839.57192	50564.42954	1.950018
58839.58271	50569.59841	2.132951
58839.59336	50566.58024	2.407460
58839.60429	50567.58993	2.580426

Data points with an asterisk have been removed from the analysis due to bad observation conditions at the beginning of the night.

Table A.5. ESPRESSO 2022 radial velocity data.

Time [BJD-2400000]	RV [$m.s^{-1}$]	σ_{RV} [$m.s^{-1}$]
59666.64409	50601.02521	0.774030
59667.60457	50600.48849	0.737487
59668.49442	50601.25985	0.694932
59671.48935	50604.68854	0.637348
59671.50020	50604.66374	0.693104
59671.51106	50605.97768	0.668581
59671.52191	50604.16692	0.652153
59671.53277	50605.78427	0.657152
59671.54363	50604.62196	0.669004
59671.55448	50604.25214	0.607821
59671.56534	50604.53055	0.645923
59671.57619	50603.13627	0.691523
59671.58705	50603.53464	0.705170
59671.59790	50603.64105	0.690240
59671.60875	50603.68365	0.738659
59671.61961	50605.29261	0.714326
59671.63047	50603.91014	0.656317
59671.64120	50604.12206	0.657496
59671.65217	50603.74764	0.766929
59671.66303	50605.54514	0.906788
59671.67501	50603.03014	0.806379
59672.48770	50604.72785	0.493576
59672.49856	50603.96418	0.501172
59672.50951	50604.29583	0.494510
59672.52027	50603.16844	0.513161
59672.53113	50605.51262	0.504788
59672.54198	50604.39121	0.494640
59672.55284	50604.02493	0.503966
59672.56369	50603.65029	0.500055
59672.57455	50606.35976	0.517452
59672.58540	50604.68079	0.521614
59672.59615	50604.55110	0.537089
59672.60711	50604.80654	0.558791
59673.59898	50601.46368	0.700858
59674.56924	50598.51450	0.518263
59675.55471	50595.66269	0.576696

Table A.4. HARPS-N 2022 radial velocity data.

Time [BJD-2400000]	RV [$m.s^{-1}$]	σ_{RV} [$m.s^{-1}$]
59671.35500	50569.37634	1.974639
59671.36610	50570.60270	2.594303
59671.37714	50572.84831	2.416007
59671.38807	50568.83393	1.968809
59671.39833	50566.43715	1.912247
59671.40906	50569.79915	1.841241
59671.41943	50570.77878	2.170695
59671.43017	50572.17411	2.417459
59671.44145	50573.60023	2.599720
59671.45198	50572.30215	2.988142
59671.46238	50566.26753	3.611159
59671.47437	50569.44185	2.866616
59671.48401	50569.47288	2.903470
59671.49522	50572.11090	1.783341
59671.50453	50572.22546	2.361605
59671.51647	50569.90146	2.690191
59671.52747	50571.63100	2.283775
59671.53769	50573.85582	2.319703